



Solving thermal issues in tensile-strained Ge microdisks

A. ELBAZ,^{1,2} M. EL KURDI,^{1,*} A. AASSIME,¹ S. SAUVAGE,¹ X. CHECOURY,¹
I. SAGNES,¹ F. BŒUF,² AND P. BOUCAUD^{1,3}

¹Centre de Nanosciences et de Nanotechnologies, CNRS, Univ. Paris-Sud, Université Paris-Saclay, Avenue de la Vauve 91120, Palaiseau, France

²STMicroelectronics, Rue Jean Monnet 38054, Crolles, France

³Present address: Université Côte d'Azur, CRHEA CNRS, Rue Bernard Grégory 06560, Valbonne, France

*moustafa.el-kurdi@u-psud.fr

Abstract: We propose to use Ge-dielectric-metal stacking to allow one to address both thermal management with the metal as an efficient heat sink and tensile strain engineering with the buried dielectric as a stressor layer. This scheme is particularly useful for the development of Ge-based optical sources. We demonstrate experimentally the relevance of this approach by comparing the optical response of tensile-strained Ge microdisks with an Al heat sink or an oxide pedestal. Photoluminescence indicates a much reduced temperature rise in the microdisk (16 K with Al pedestal against 200 K with SiO₂ pedestal under a 9 mW continuous wave optical pumping). An excellent agreement is found with finite element modeling of the temperature rise. This original stacking combining metal and dielectrics is promising for integrated photonics where thermal management is an issue.

© 2018 Optical Society of America under the terms of the [OSA Open Access Publishing Agreement](#)

1. Introduction

Semiconductor-on-insulator substrates, in particular Silicon-On-Insulator, have been extensively used for the development of integrated optical components in the near-infrared and more recently for the mid-infrared [1], enabling emerging CMOS-compatible photonics technologies. The combination of low cost of fabrication, ability to be produced on very large scale wafers and high index contrasts allowing strong optical confinement has strongly facilitated the development of Si-photonics applications [2]. Thermal management remains however an issue, particularly with the emergence of active functionalities requiring high pumping densities for nonlinear processes, either light generation or integrated full-optical signal processing [3,4]. This is in part due to the low thermal conductivity of the buried oxide layer, as commonly used in silicon-on-insulator (SOI) or germanium-on-insulator (GOI) [5] substrates on which optical components are developed. This low thermal conductivity limits the efficient thermal cooling from the active layer to the substrate. This situation is even worse for free-standing layers as required by design optimization for tensile-strained engineered Ge [6–9].

These past years, strong efforts were indeed devoted to strain engineering on GeSn [10] and more extensively on pure Ge with the aim to demonstrate a laser, operating up to room temperature in continuous wave (CW) mode [11,12]. Strain engineering can help to reach a direct band gap configuration [13,14]. The microdisk geometry has been extensively used in strain engineering of Ge, since it is one of the most obvious way to induce large biaxial strain transfer to the Ge layers using stressor layers. With strained microdisks, high optical gain can be expected while taking advantage of the high Q-factor whispering gallery modes for resonant coupling to stimulated emission. Promising methods were employed to induce high tensile strain transfer using external film stressors in both pure Ge [15–18] and GeSn active layers [19–21]. There is however a penalty induced by strain engineering and the associated

process flow. Thermal cooling is strongly quenched by using either dielectrics like SiO_2 or suspended mushroom-type structures [22,16]. This decreased thermal cooling has a strong impact on the performances of laser devices.

Here, we show that an approach combining dielectrics and metal can provide simultaneously strain and thermal management and meanwhile allows one to keep the high index contrast in the semiconductor-dielectric part of the stacking. This approach results in tensily-strained Ge microdisks fabricated on metallic pedestals.

2. Experiments

An 850 nm thick Ge layer is grown in an industrial RPCVD (Reduced Pressure Chemical Vapor Deposition) reactor on a 12 inches SOI wafer substrate with a buried oxide (BOX) thickness of 740 nm and a top Si thickness of 200 nm. In the first step of the fabrication, several layers that compose the bottom stacking after bonding are deposited. As shown in Figs. 1(a)-1(c), a 400 nm thick silicon nitride layer is first deposited by plasma enhanced chemical vapor deposition (PECVD). The silicon nitride layer is compressively strained and is used as a bottom stressor layer. Then, two types of samples were prepared, one with a 700 nm thick silicon dioxide layer and deposited by PECVD, and a second one with an aluminum layer with the same thickness deposited using an e-beam evaporation technique [Fig. 1(b)]. In both cases, a gold layer is finally deposited for bonding on a host Si substrate using gold-gold thermo-compressive bonding method [Fig. 1(c)]. For the specific case of Al, a thin silicon nitride barrier (50 nm) is deposited prior to the gold deposition to avoid interdiffusion of gold into Al during the bonding process at 300°C . After bonding, the SOI substrate is removed by mechanical polishing and dry inductively-coupled-plasma etching, the BOX of the SOI substrate serving as an etch-stop layer. This etch stop is removed using dilute hydrofluoric acid solution. The 200 nm thick silicon layer of the SOI is removed with the defective Ge/Si interface in a single step using non-selective dry etching process, allowing to thin the Ge layer down to a final thickness of 350 nm. After this non-selective etching process to remove the Ge/Si interface and thin the Ge layer, we obtain a quite smooth surface, as shown in Fig. 1(g). Finally, we obtain a Ge/ Si_xN_y /Al stacking, or Ge/ Si_xN_y / SiO_2 stacking as shown in Fig. 1(g). Then, a standard processing using e-beam lithography, dry etching and selective wet etching is performed to realize standing Ge/ Si_xN_y disks on silicon dioxide or Al pedestal [Figs. 1(d)-1(f), and 1(h)]. For Al etching we used a Potassium Hydroxide (KOH) base solution as etchant. The etchant is highly selective with respect to Ge and we did not observe any change of the Ge layer thickness or surface roughness after the etch of Al. While processing the microdisk on both types of samples, a special attention was dedicated to obtain a pedestal with different materials but with equivalent diameters for each type of sample. In our comparative study between both types of samples, we estimate the pedestal diameter around $4\ \mu\text{m}$ for $8\ \mu\text{m}$ disk diameters.

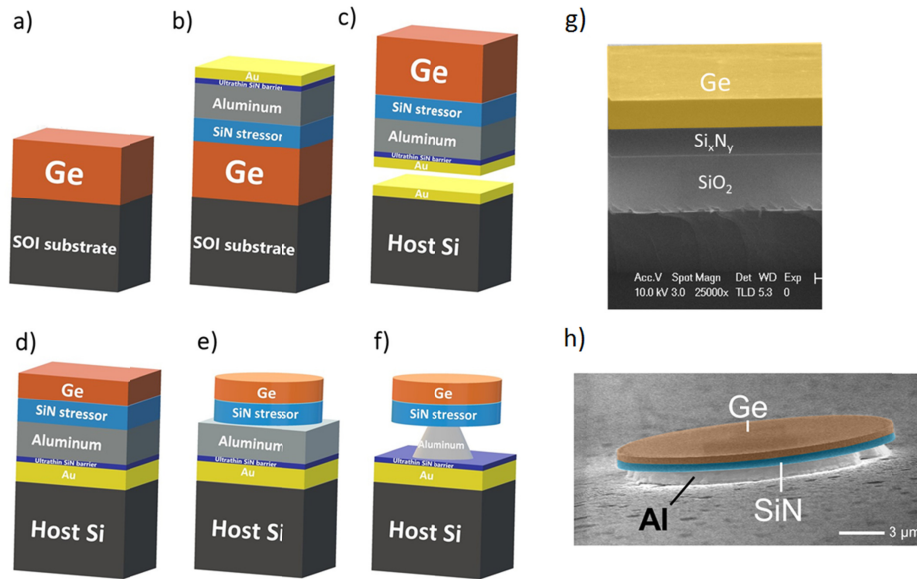


Fig. 1. Description of the processing steps (a) Ge was first grown on a silicon-on-insulator substrate using RPCVD method. (b) The germanium layer is then covered by a silicon nitride film, then by an Al or SiO₂ (not shown) film, and finally by an ultrathin silicon nitride layer followed by a gold layer deposition. (c) The Ge-on-insulator is then bonded on a host silicon substrate, by Au-Au thermo-compressive bonding, then the SOI substrate is removed (d) The Ge film is etched to a thickness of 350 nm. (e) The microdisks are patterned by electronic lithography and plasma etching. (f) A selective underetching is finally used to form the aluminum pedestal. (g) SEM view of photonic stacking after step d) but with a SiO₂ layer instead of Al (h) Example of a scanning electron microscopy image of a processed microdisk on an aluminum post.

Room temperature photoluminescence experiments are conducted on the Ge disks of the same size on both types of samples, i.e. with aluminum post and silicon dioxide post. A continuous wave HeNe laser pump at 632.8 nm wavelength is focused on the disk center using a 3.5 μm spot diameter with a x50 objective, the emission from the Ge microdisk is collected with the same objective and analyzed with a monochromator coupled to a liquid nitrogen cooled InGaAs extended CCD detector. The experiments were not performed on structures with all-around stressors since it leads to red-shift of the emission beyond the detector cut-off. Figure 2 shows the emission spectrum of the Ge disk with an Al post [Fig. 2(a)] in comparison with the Ge disk with a SiO₂ post at various optical pump power [Fig. 2(b)].

In both cases, the emission spectrum is dominated by the direct band gap transitions. The direct emission which occurs at 1530 nm for relaxed Ge layer is red-shifted to longer wavelength due to the tensile strain transferred from the bottom silicon nitride layer. Interestingly, the emission occurs at longer wavelength, 1755 nm, for the disk with the Al post as compared to the oxide post case with an emission maximum occurring at 1673 nm. A finite element method (FEM) calculation of elastic strain in a disk with an oxide post and with a single stressor layer gives an average equivalent biaxial tensile strain of 0.68%. An equivalent value is found by FEM with an Al post, since Al exhibits a Young modulus equivalent to the one of SiO₂ (70 GPa). The in-plane tensile strain profile along the disk diameter varies between a maximum value of 1% and a minimum value of 0.5%. The fundamental direct band gap energy can be independently calculated in the framework of a 30 band **k.p** model accounting for biaxial tensile strain [13]. The maximum of photoluminescence at 1673 nm (SiO₂ post) and 1755 nm (Al post) can be modeled assuming a

biaxial tensile strain of 0.65% and 0.85% respectively. There is thus a very good agreement between modeling and experiments for SiO₂ posts. The longer emission wavelength as observed with Al post can be explained by the ductile mechanical characteristics of Al that are not taken into account in our FEM modelling in the framework of Hooke's laws. Plastic behavior of pure Al should be attained for yield stress as low as 10 MPa - 50 MPa to be compared with the 2 GPa of built-in stress for the SiN layer. Plastic behavior of Al should be responsible for larger relaxation of the built-in compressive stress of the SiN layer after patterning into suspended disks thus inducing more tensile strain transfer to the upper Ge layer.

In both cases of Al and oxide posts, the spectrum exhibits low Q-factor resonances that are assigned to quasi-radial modes present in the disk cavity. These modes exhibit low azimuthal number, and behave like Fabry-Perot modes constructed by secular reflection at the disk edges. The low Ge/Air reflectivity is responsible of low Q-factors for Fabry-Perot modes in these micrometer-size cavities. On the photoluminescence spectra, the modes are well defined for both the SiO₂ and Al posts in the 1750-1850 nm wavelength range. The mode positions are found at 1760 (1768) nm, 1792 (1796) nm, 1831(1828) nm on the photoluminescence spectra with SiO₂ (Al) posts. The mode spacing and wavelength positions are consistent with those expected from quasi-radial modes analysis using Eq. (1) of [23], considering a disk diameter of 8 μm and an effective index of 3.6 for TE₀ first-order vertical mode and 2.4 (TE₁) for the 350 nm thick Ge layer in TE polarization. We consider TE polarization since it should be preferentially collected in the setup configuration, i. e. collection of emission from the top surface of the disk. The analysis in [23] is performed in a 2D analytical model considering quasi-radial modes, exhibiting small azimuthal index (m) with respect to radial index (n) i.e. $n \gg m$. In this case the resonant wavelength $\lambda_{n,m}$ can be approximated into an analytical expression only depending on the index (n,m), the disk radius and the effective index of vertically confined waves propagating in the Ge layer. From Eq. (1) of [23] we obtain resonant wavelengths at 1772 nm, 1789 nm and 1830 nm, that can be associated to TE₀ (16,1), TE₁ (10,2) and TE₀ (15,2) respectively in quite good agreement with the experimentally observed mode positions. Note that these mode positions may vary by typically only +/- 10nm for different combinations of (n,m) providing that the $2n + m$ value is kept constant. We note that whispering gallery modes are not observed in the photoluminescence spectra of Fig. 2. This is not assigned to optical losses induced by the Al post, but rather to the experimental conditions. First the pump beam being aligned with the disk center leads to a poor overlap between light generation and optical field of confined whispering gallery modes, the latter being mainly distributed at the disk edges. Secondly whispering gallery modes are quenched by the direct band absorption and can thus only be clearly observed above 1800 nm in a range where the signal to noise ratio is smaller. Thirdly higher spectral resolution is needed and would require longer acquisition times. Note that in [11] equivalent Q-factor values of more than 5000 were obtained for WGMs lasing modes in Ge microdisks with Al pedestals as used in the present work. The underetched aluminum layer does not limit the Q-factors as well as the dry etch process to thin the Ge layer. In [11], optical gain was achieved on direct band transitions, thanks to higher tensile strain applied using a second stressor layer deposited on the top surface of the Ge disk.

On Fig. 2, we observe a strong red-shift of the emission maximum for the Ge disk with an oxide post while the incident beam power is increased. We can assign this red-shift of the direct band gap to an increase of the temperature in the disk. At low incident pumping power, the emission amplitudes are quasi-similar, 950 intensity counts for Al post and 730 counts with the oxide post. However, as the pump power is increased, the emission from the Ge disk with Al post follows a stronger increase than the one observed with the oxide post such that at higher pump power, 19 500 counts are reached at the maximum signal for the Al post against 11 000 counts for the oxide post at 9.1 mW incident pump power. This difference can be explained by a reduction of the quantum efficiency in the Ge disk with the temperature rise.

Additionally, the emission width increases from 168 nm up to 199 nm with the Al post, while it increases from 174 nm up to 320 nm with the oxide post. This significant broadening of the emission spectrum is a consequence of carrier energy distribution spreading in the valence and conduction bands. The temperature rise induces an enhancement of scattering and broadening effects detrimental to radiative recombination process in these luminescent structures. The temperature rise, broadening increase and reduction of emission efficiency are quasi-systematically observed with Ge-on-dielectric layer cavities, thus limiting strongly the incident pump power that can be used. It can even in some cases lead to damages to the layer under high optical pumping, which is not the case with the Al pedestal disk that sustains much higher excitation powers. We emphasize that this property is a key feature that would allow future devices to be pumped at high excitation densities without significant heating effects and more importantly in CW regime.

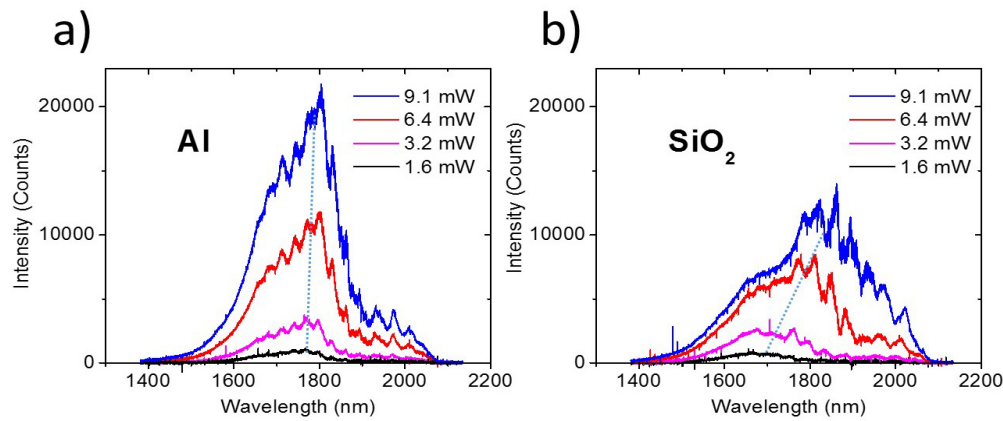


Fig. 2. (a) CW emission spectra at 300 K of a 8 μm diameter microdisk with an aluminum pedestal, for various optical pump powers. (b) CW emission spectra at 300 K of a 8 μm diameter microdisk with a silicon dioxide pedestal, for various excitation densities. The blue dotted line are given as a guide to follow the emission maximum. 9.1 mW corresponds to an intensity of 95 kW cm^{-2} .

3. Modeling

A finite element analysis of the thermal heating in both types of samples was performed using commercially available software (COMSOL). We represent the temperature mapping in Fig. 3. The substrate temperature is fixed at 300 K, and a 2D axisymmetric geometry is used. The pumping power is considered as a homogeneous heating source deposited at the center of the disk. The heat source has the same diameter as the spot diameter (3.5 μm) and is extended into 50 nm depth in the Ge layer corresponding to the absorption length at the pump wavelength (632.8 nm). The heating power density is $1.9 \times 10^{16} \text{ W/m}^3$, assuming a reflection coefficient of 0.45 at the Air/Ge interface at the pump wavelength, and a 9.1 mW of incident optical power. Here the strained Ge exhibits an indirect band alignment, with a small radiative recombination rate. We can thus assume that non-radiative recombination process dominate and that the entire absorbed power is transformed into heating. This was confirmed by performing experiments using a longer pump wavelength at 1064 nm closer to the band gap. Similar experimental results were obtained in the latter case.

Due to the very high difference of thermal conductivity for aluminum (220 W/(m.K)) and silicon dioxide (1.4W/(m.K) at room temperature), a clear difference in temperature reached at equilibrium is observed. The maximum temperature rise in the Ge layer on Al post is only 16 K against 200 K when a SiO_2 post is used. Interestingly, the temperature mapping of the Ge disk with the silicon dioxide post shows a strong temperature gradient within the post,

connecting the substrate to the disk. This is a consequence of the thermal flux through the disk pedestal. Since it exhibits a low conductivity, the oxide post is strongly limiting the heat transfer between the substrate and the Ge layer, explaining the high temperature reached. A ring shape of the incident power distribution on the disk surface can be helpful to optimize the overlap between the excited gain region and the whispering gallery modes. In this situation considering a ring shape of 1.75 μm width and 4.5 μm inner diameter, the temperature rise is much more pronounced, since it attains 615 K in the Ge disk layer with a silicon dioxide post. Such high temperature increase prevents in practice any use of such pumping scheme on disk while with the Al post the temperature rise is significantly reduced with only 55 K of temperature increase. Moreover, the difference between oxide pedestal and aluminum pedestal is even more important at cryogenic temperature. Indeed, the thermal conductivity of the silicon dioxide decreases with the temperature, from 1.4 W/(m.K) at room temperature down to 0.1 W/(m.K) at 4 K [18], leading to an even worse behavior at cryogenic temperatures. On the contrary, the aluminum thermal conductivity is correlated with electronic conductivity and increases at low temperature, as it is the case in many metals. It can reach a maximum value of 4500 W/(m.K) at 15 K [24]. The implementation of an aluminum pedestal is thus even more beneficial at low temperature.

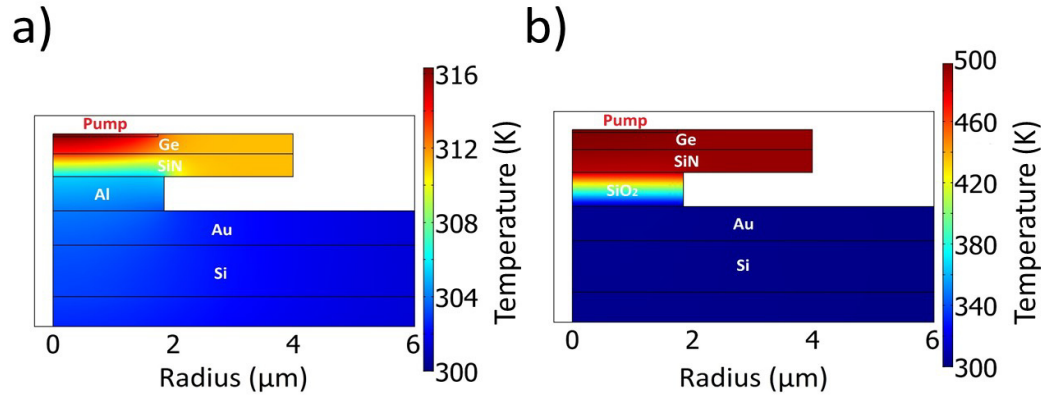


Fig. 3. (a) Distribution of temperature for a microdisk with an aluminum pedestal, with a substrate temperature of 300K, under optical excitation at 633 nm wavelength (9.1mW incident power). The temperature only reaches 316 K. (b) Same mapping with a silicon dioxide pedestal. The temperature reaches 500 K in the same pumping conditions.

4. Discussion

In Fig. 4, we show a comparison between the average temperature reached in the disk as calculated by FEM analysis and the one we estimated from the experimental data. For that purpose, we measured the direct band gap emission red-shift from the PL spectrums as shown in Fig. 2. Once we determined this red-shift for every pump powers applied, we just deduce the increase of temperature using Varshni's Law [25], which describes the band gap energy dependence with the temperature as:

$$E_{gap}(T) = E_{G,0} - \frac{\alpha T^2}{T + \beta} \quad (1)$$

We set α to 5.82×10^{-4} eV/K, β to 296 K following [26]. We assume that these parameters are weakly dependent with strain. $E_{G,0}$ is red-shifted from 0.89 eV [26] to 0.8 eV for the sample with the Al post and 0.84 eV for the sample with the oxide post to account for the red

shift of the emission as observed experimentally with respect to unstrained Ge at room temperature.

As can be seen in Fig. 4, a very good agreement is obtained between experimental results and the modelling. This good consistency indicates that the impact of metallic layer can be predicted with a good degree of confidence with modeling. It can thus enable the design of more complex photonic structures with appropriate thermal management.

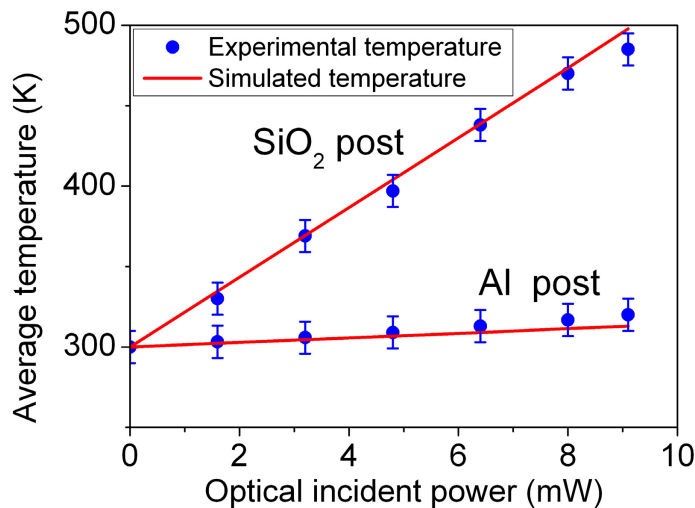


Fig. 4. Temperature in the microdisks with Al and SiO₂ pedestal respectively as a function of the incident optical power. The blue disks report the experimental temperature deduced from measurement of the red-shift of the band gap extracted from photoluminescence [Fig. 2]. The red lines represent the average temperature calculated by finite element analysis (two-dimensional mapping of temperature is shown on Fig. 3 for an incident optical power of 9.1 mW). The error bars represent the uncertainty due to the experimental measurement from the direct band-gap emission red shift.

5. Conclusion

In conclusion, we have presented a novel photonic stacking that allows to both manage an efficient strain engineering and an excellent thermal cooling based on the introduction of a metallic layer as heat sink. This method is appropriate for the design of microresonators like microdisks. We show that a large reduction of thermal heating in Ge microdisk cavities under CW pumping can be achieved by typically one order of magnitude when an Al pedestal is used as replacement of a SiO₂ pedestal. Beyond thermal aspects, the semiconductor-dielectric-metal heterostructure as presented in this work would also be compatible with the design of electrodes for vertical current injection through the Al pedestal into the semiconductor active layer [27], that cannot be addressed in standard semiconductor-dielectric photonic stacking. A possible topology could be a central metallic post to contact the bottom n-type Ge layer. We emphasize that this method is not restricted to Ge-based semiconductors, since silicon [28] or III-V materials can as well take advantage of the high index contrast provided by the semiconductor-dielectric stacking and better thermal management with dielectric on metal [29].

Funding

Agence Nationale pour la Recherche; Association Nationale de la Recherche et de la Technologie.

Acknowledgements

We acknowledge support from the RENATECH network and funding of Anas Elbaz from Association Nationale de la Recherche et de la Technologie (ANRT) and CIFRE grants. This work was supported by Agence Nationale pour la Recherche under ELEGANTE convention (AAP-17-CE24-0015), and as part of the “Investissements d’Avenir” program (reference: ANR-10-LABX-0035, Labex NanoSaclay).”

References

1. R. Soref, “Mid-infrared photonics in silicon and germanium,” *Nat. Photonics* **4**(8), 495–497 (2010).
2. D. Thomson, A. Zilkie, J. E. Bowers, T. Komljenovic, G. T. Reed, L. Vivien, D. Marris-Morini, E. Cassan, L. Virost, J.-M. Fédéli, J.-M. Hartmann, J. H. Schmid, D.-X. Xu, F. Boeuf, P. O’Brien, G. Z. Mashanovich, and M. Nedeljkovic, “Roadmap on silicon photonics,” *J. Opt.* **18**(7), 073003 (2016).
3. B. Kuyken, H. Ji, S. Clemmen, S. K. Selvaraja, H. Hu, M. Pu, M. Galili, P. Jeppesen, G. Morthier, S. Massar, L. K. Oxenlowe, G. Roelkens, and R. Baets, “Nonlinear properties of and nonlinear processing in hydrogenated amorphous silicon waveguides,” *Opt. Express* **19**(26), B146–B153 (2011).
4. H. El Dirani, C. Monat, S. Brisson, N. Olivier, C. Jany, X. Letartre, M. Pu, P. D. Girouard, L. H. Frandsen, E. Semenova, L. K. Oxenlowe, K. Yvind, and C. Sciancalepore, “SiNOI and AlGaAs-on-SOI nonlinear circuits for continuum generation in Si photonics,” in *Proc. SPIE 10535, Integrated Optics: Devices, Materials, and Technologies XXII*, (2018), Vol. 10535, pp. 1053508–10535–9.
5. X. Xu, H. Hashimoto, K. Sawano, and T. Maruizumi, “Highly n-doped germanium-on-insulator microdisks with circular Bragg gratings,” *Opt. Express* **25**(6), 6550–6560 (2017).
6. M. J. Süess, R. Geiger, R. A. Minamisawa, G. Schiefler, J. Frigerio, D. Chrastina, G. Isella, R. Spolenak, J. Faist, and H. Sigg, “Analysis of enhanced light emission from highly strained germanium microbridges,” *Nat. Photonics* **7**(6), 466–472 (2013).
7. A. Gassenq, K. Guillo, G. Osvaldo Dias, N. Pauc, D. Rouchon, J.-M. Hartmann, J. Widiez, S. Tardif, F. Rieutord, J. Escalante, I. Duchemin, Y.-M. Niquet, R. Geiger, T. Zabel, H. Sigg, J. Faist, A. Chelnokov, V. Reboud, and V. Calvo, “1.9% bi-axial tensile strain in thick germanium suspended membranes fabricated in optical germanium-on-insulator substrates for laser applications,” *Appl. Phys. Lett.* **107**(19), 191904 (2015).
8. D. Nam, D. S. Sukhdeo, J.-H. Kang, J. Petykiewicz, J. H. Lee, W. S. Jung, J. Vučković, M. L. Brongersma, and K. C. Saraswat, “Strain-Induced Pseudoheterostructure Nanowires Confining Carriers at Room Temperature with Nanoscale-Tunable Band Profiles,” *Nano Lett.* **13**(7), 3118–3123 (2013).
9. D. Nam, D. S. Sukhdeo, S. Gupta, J.-H. Kang, and M. L. Brongersma, and K. C. Saraswat, “Study of Carrier Statistics in Uniaxially Strained Ge for a Low-Threshold Ge Laser,” *IEEE J. Sel. Top. Quantum Electron.* **20**(4), 16–22 (2014).
10. S. Wirths, R. Geiger, N. von den Driesch, G. Mussler, T. Stoica, S. Mantl, Z. Ikonc, M. Luysberg, S. Chiussi, J. M. Hartmann, H. Sigg, J. Faist, D. Buca, and D. Grützmacher, “Lasing in direct-bandgap GeSn alloy grown on Si,” *Nat. Photonics* **9**(2), 88–92 (2015).
11. A. Elbaz, M. El Kurdi, A. Aassime, S. Sauvage, X. Checoury, I. Sagnes, C. Baudot, F. Boeuf, and P. Boucaud, “Germanium microlasers on metallic pedestals,” *APL Photon.* **3**(10), 106102 (2018).
12. S. Bao, D. Kim, C. Onwukaeme, S. Gupta, K. Saraswat, K. H. Lee, Y. Kim, D. Min, Y. Jung, H. Qiu, H. Wang, E. A. Fitzgerald, C. S. Tan, and D. Nam, “Low-threshold optically pumped lasing in highly strained germanium nanowires,” *Nat. Commun.* **8**(1), 1845 (2017).
13. M. El Kurdi, G. Fishman, S. Sauvage, and P. Boucaud, “Band structure and optical gain of tensile-strained germanium based on a 30 band kp formalism,” *J. Appl. Phys.* **107**(1), 013710 (2010).
14. D. S. Sukhdeo, D. Nam, J.-H. Kang, M. L. Brongersma, and K. C. Saraswat, “Direct bandgap germanium-on-silicon inferred from 57% (100) uniaxial tensile strain [Invited],” *Photon. Res.* **2**(3), A8–A13 (2014).
15. G. Capellini, G. Kozłowski, Y. Yamamoto, M. Lisker, C. Wenger, G. Niu, P. Zaumseil, B. Tillack, A. Ghrib, M. de Kersauson, M. El Kurdi, P. Boucaud, and T. Schroeder, “Strain analysis in SiN/Ge microstructures obtained via Si-complementary metal oxide semiconductor compatible approach,” *J. Appl. Phys.* **113**(1), 013513 (2013).
16. A. Ghrib, M. El Kurdi, M. de Kersauson, M. Prost, S. Sauvage, X. Checoury, G. Beaudoin, I. Sagnes, and P. Boucaud, “Tensile-strained germanium microdisks,” *Appl. Phys. Lett.* **102**(22), 221112 (2013).
17. A. Ghrib, M. El Kurdi, M. Prost, S. Sauvage, X. Checoury, G. Beaudoin, M. Chaigneau, R. Ossikovski, I. Sagnes, and P. Boucaud, “All-Around SiN Stressor for High and Homogeneous Tensile Strain in Germanium Microdisk Cavities,” *Adv. Opt. Mater.* **3**(3), 353–358 (2015).
18. M. El Kurdi, M. Prost, A. Ghrib, S. Sauvage, X. Checoury, G. Beaudoin, I. Sagnes, G. Picardi, R. Ossikovski, and P. Boucaud, “Direct Band Gap Germanium Microdisks Obtained with Silicon Nitride Stressor Layers,” *ACS Photonics* **3**(3), 443–448 (2016).
19. X. Chen, C. S. Fenrich, M. Xue, M.-Y. Kao, K. Zang, C.-Y. Lu, E. T. Fei, Y. Chen, Y. Huo, T. I. Kamins, and J. S. Harris, “Tensile-strained Ge/SiGe multiple quantum well microdisks,” *Photon. Res.* **5**(6), B7–B14 (2017).
20. S. Liu, K. Peng, H. Zhan, L. Ni, X. Wang, Y. Wang, Y. Li, J. Yu, L. Jiang, R. Zhu, J. Wang, F. Jing, and A. Lin, “3 kW 20/400 Yb-Doped Aluminophosphosilicate Fiber With High Stability,” *IEEE Photonics J.* **10**(5), 1–8 (2018).

21. R. W. Millar, D. C. S. Dumas, K. F. Gallacher, P. Jahandar, C. MacGregor, M. Myronov, and D. J. Paul, "Mid-infrared light emission $> 3 \mu\text{m}$ wavelength from tensile strained GeSn microdisks," *Opt. Express* **25**(21), 25374–25385 (2017).
22. A. Z. Al-Attili, S. Kako, M. K. Husain, F. Y. Gardes, N. Higashitarumizu, S. Iwamoto, Y. Arakawa, Y. Ishikawa, H. Arimoto, K. Oda, T. Ido, and S. Saito, "Whispering Gallery Mode Resonances from Ge Micro-Disks on Suspended Beams," *Front. Mater.* **2**, 43 (2015).
23. M. El Kurdi, M. Prost, A. Ghrib, A. Elbaz, S. Sauvage, X. Checoury, G. Beaudoin, I. Sagnes, G. Picardi, R. Ossikovski, F. Boeuf, and P. Boucaud, "Tensile-strained germanium microdisks with circular Bragg reflectors," *Appl. Phys. Lett.* **108**(9), 091103 (2016).
24. H. M. Rosenberg, "The thermal conductivity of metals at low temperatures," *Philos. Trans. R. Soc. Lond. Ser. Math. Phys. Sci.* **247**(933), 441–497 (1955).
25. Y. P. Varshni, "Band-to-Band Radiative Recombination in Groups IV, VI, and III-V Semiconductors (I)," *Phys. Status Solidi, B Basic Res.* **19**(2), 459–514 (1967).
26. M. E. Levinstein, S. L. Romyantsev, and M. Shur, "SILICON (Si)," in *Handbook Series on Semiconductor Parameters* (WORLD SCIENTIFIC, 1996), pp. 1–32.
27. M. Prost, M. El Kurdi, A. Ghrib, S. Sauvage, X. Checoury, N. Zerounian, F. Aniel, G. Beaudoin, I. Sagnes, F. Boeuf, and P. Boucaud, "Tensile-strained germanium microdisk electroluminescence," *Opt. Express* **23**(5), 6722–6730 (2015).
28. C. Lacava, M. A. Ettabib, and P. Petropoulos, "Nonlinear Silicon Photonic Signal Processing Devices for Future Optical Networks," *Appl. Sci. (Basel)* **7**(1), 103 (2017).
29. M. Pu, L. Ottaviano, E. Semenova, and K. Yvind, "Efficient frequency comb generation in AlGaAs-on-insulator," *Optica* **3**(8), 823–826 (2016).